Vorticity produced by shock wave diffraction

S. Sivier[1], E. Loth[1], J. Baum[2] and R. Löhner[3]

[1] Department of Aeronautical and Astronautical Engineering, University of Illinois at Urbana-Champaign, Urbana Il 61801, USA
[2] Science Applications International Corporation, McLean VA 22102, USA
[3] CMEE School of Engineering and Applied Science, The George Washington University, Washington D.C. 20052, USA

Abstract. Numerical simulations with a monotonicity preserving flow solver have been performed to study shock diffraction phenomena and shock wave generated vorticity. The computations were performed using the conservative Finite Element Method-Flux Corrected Transport (FEM-FCT) scheme, which has been shown to have an excellent predictive capability for various compressible flows with both strong and weak shocks. An adaptive unstructured methodology based on adapting to high density and entropy gradients was used in conjunction with a conservative shock-capturing scheme to adequately resolve strong and weak flowfield gradients. The chief interest was the formation of vorticity arising from shock wave propagation over a sharp corner and the high accuracy and resolution of the interacting compressible wave features. Numerical simulations were compared with previous experimental results and exhibited remarkably good agreement in terms of compressible wave propagation, as well as vorticity development and transport. The computations also allowed insight into the fundamental fluid dynamics, specifically shock diffraction, vortex convection and shock-vortex interactions.

Key words: Vorticity, Shock diffraction, CFD

1. Introduction

The propagation and diffraction of shocks past solid bodies has received considerable attention in the past, both experimentally and computationally. While much emphasis has been placed on the various types of reflections resulting from two- and three-dimensional inclined planes and cylinders, direct investigation of the vorticity produced from shocks passing sharp corners has not been fully addressed. Despite the short time evolution of the shock diffraction phase, it is expected that such production may play a significant role on the resulting surface pressure distribution. For reviews related to this subject, see Glaz et al. (1985), Glass et al.

(1990) and Sivier (1991). Some recent studies are discussed in the following.

1.1. Previous experimental studies

Mandella et al. (1985) conducted a number of experiments to examine shock generated vortices around sharp corners. In the study, vortices are formed by shock waves passing over obstacles such as wedges or around corners. Much of the study concentrated on investigation symmetrical trailing edge vortices formed off backward facing steps as a narrow channel suddenly expands into a large two-dimensional section. Results for a shock Mach number of 1.36 were presented. The pressure in the vortex was found to be less than 30% of the pressure at the outer edge. The experiments showed that the flow may be supersonic (with a Mach number near 1.7) near the center of the vortex while being subsonic (with a Mach number near 0.6) in the external flow. The study was unable to resolve any of the viscous flow effects near the centers of the vortices. In addition, it was noted that inviscid effects govern vorticity generation behind curved shocks due to the baroclinic effect.

Howard and Mathews (1956) presented interferogram studies of shocks passing over a 5° vertical wedge and the subsequent vortices produced. The photographs showed the well developed spiral slip layer which subsequently developed secondary eddies whose strength and frequency were found to be approximately independent of shock strength or static pressure.

Studies by Ben-Dor and Glass (1980) and by Heilig and Reichenbach (1983) examined a number of shocks with various strengths impinging on wedges of various angles. The studies examined the effect of shock Mach number and wedge angle on the type of reflection that occurred as the shock hit the wedge. There were four types of reflection found to occur: regular reflection and three types of irregular reflection: single Mach reflection, complex Mach reflection and double Mach reflection

Studies by Schardin (1957, 1966) included high speed cinematography in order to examine a shock wave impinging

Correspondence to: E. Loth

on a wedge. The result was a series of shadowgraphs which clearly showed the diffraction of a Mach 1.3 shock as it passed the wedge, and the resulting vortex on the back face of the wedge as well as shock/vortex interactions. This study provided a high quality experimental basis for the present computational work, and its results will be discussed along the those of the current study.

1.2. Previous numerical and analytical studies

Howard and Mathews (1956) developed an inviscid theoretical description of the vortex development for weak shocks in polar coordinates. The flow was assumed to be isentropic (and thus free of discontinuities such as shocks or slip layers), pseudo-stationary, and symmetrical about the origin. Based on these assumptions, the authors showed that the vortex development was conical in nature, i.e. the normalized radial distribution of density was shown to be time invariant for a given Mach number downstream of the shock. This was validated by experimental work in the same study. A second semi-empirical theory was also used to predict the rate of growth of the vortex and yielded rates roughly 10% below that of the experiment. Limitations of the work were pointed out to be the neglection of slip layers and the neglection of viscous effects, which were probably responsible for the poor agreement for the density very near the center of the vortex. Merzkirch (1964) extended this theoretical work to include a viscous vortex core which yielded improved agreement with experiment near the vortex center.

Numerical methods have increasingly been used to perform studies similar to the above experimental studies. Aso et al. (1990) used a total variation diminishing (TVD) scheme to investigate the various types of reflections noted above that occur when a shock impinges on a wedge in two-dimensional Euler flow similar to the experimental studies presented by Ben-Dor and Glass (1980) and by Heilig and Reichenbach (1983). In the second part of the study, viscous effects were added by using the thin-layer approximated Navier-Stokes equations for direct comparison with the Euler solutions. The convection terms were implemented with the TVD scheme while the viscous terms used a conventional central difference scheme. It was found that for weak shocks, results were very similar, although the height of the Mach stem was found to decrease as a boundary layer flow was added and as the Reynolds number decreased.

A study by Meadows et al. (1991) used a second order upwind finite volume scheme to solve the two-dimensional Euler equations. This method was used in order to capture shocks without any accompanying numerical oscillations. The scheme was applied to the flow of a clockwise rotating vortex as it convected from the left, upstream side of the numerical domain into a stationary shock. The computation used a hybrid vortex model where the vortex core rotates with constant velocity and the velocity decays exponentially outside the core. As the vortex impinges on the shock, two pressure regions form; a higher pressure region above the vortex center, and a lower pressure region below the vortex center. The region of high pressure occurs where the velocity induced on the shock by the vortex causes the shock

to shift downstream, resulting in a compressed flow downstream. Similarly, the region of low pressure occurs where the velocity induced on the shock by the vortex causes the shock to move upstream, expanding the flow. While the computed flowfield and its associated acoustic field agreed qualitatively with experiments, the authors felt that improvements, including higher order methods and grid adaptation, would be required for accurate quantitative results.

The flux corrected transport scheme has been shown to be highly robust and accurate for several fluid dynamics problems in the context of finite-element schemes (Löhner et al. 1987, 1989; Baum et al. 1990; Loth et al. 1990a, 1990b). Studies by Baum et al. (1990) used the FEM-FCT scheme combined with an adaptive refinement method to examine a shock wave impinging on canisters elevated over two support beams. These studies demonstrated the advantages of using an adaptive grid: mesh refinement occurred upstream of all shocks and along contact discontinuities, and subsequently coarsened as these features passed through the grid – thus providing high resolution only in areas of significant flow gradients. The results also showed that FEM-FCT was capable of capturing shocks without generating numerical oscillations. Some of the more interesting flow features found in the computation were shock reflection and the formation of vortices at the sharp cornered support beams. In addition, an axisymmetric version of FEM-FCT with an additive grid scheme was used by Loth et al. (1990b) to examine a compressible unsteady separated flow: supersonic flow over an axisymmetric backward facing step. Good agreement of time averaged surface pressure distributions with experiment was noted on the base wall and along the reattachment wall for several configurations and upstream Mach numbers, indicating the primary flow physics were successfully modeled.

1.3. Current study

Based on previous studies (Baum et al. 1990; Loth et al. 1990b), the premise of this work is that the Euler FEM-FCT simulations for which the separation point can be specified (to occur at sharp rearward corners) will produce a reasonable representation of unsteady wall pressures for a shock wave diffraction process. Successful modeling of such transient pressures behind generic sharp corners is important to allow efficient and robust simulations of blast wave propagation past complex three-dimensional objects. The advantage of gas dynamic large eddy simulations is clear when one considers the alternative – direct simulations of the full three-dimensional unsteady Navier-Stokes equations for complex bodies, which appear impractical given current or near term capabilities of modern supercomputers.

The current study examines, through FEM-FCT, the two-dimensional, unsteady problem of a Mach 1.3 wave impinging on a 55° wedge, which was the subject of a flow visualization experiment by Schardin (1966). This shock speed is just above the weak shock regime (Obermeier and Handke 1990). Computing such a flowfield allows direct comparison with experimental results, insight into the fundamental fluid physics of near weak shock wave diffraction

past a sharp corner, and allows evaluation of the proposed phenomenological approach for robustness, resolution and accuracy.

2. Numerical method

2.1. Transport equations

The following is a brief summary of the numerical method and the implementation used in this study; for more detail see Sivier (1991). The governing equations for this flow are written in conservation form (Löhner et al. 1987) as

$$\frac{\partial \mathbf{U}}{\partial t} + \frac{\partial \mathbf{F}_j}{\partial x_j} = 0 \qquad (1)$$

where the summation convention is used and

$$\mathbf{U} = \begin{bmatrix} \rho \\ \rho u_i \\ \rho e \end{bmatrix}, \qquad \mathbf{F}_j = \begin{bmatrix} \rho u_j \\ \rho u_i u_j + p\delta_{ij} \\ u_j(\rho e + p) \end{bmatrix} \qquad (2)$$

and the state equations are

$$p = (\gamma - 1)\rho[e - 1/2u_j u_j], \quad T = [e - 1/2u_j u_j]C_v \qquad (3)$$

where ρ, p, e, T, k, γ and C_v are density, pressure, specific total energy, temperature, thermal conductivity of the fluid, ratio of specific heats, and specific heat at constant volume, respectively, and u_i is the component of the fluid velocity in the direction x_i of a Cartesian coordinate system. Thus, the fluid is assumed to be compressible and inviscid (although artificial viscosity is present in the numerical scheme).

The higher order solution chosen for FEM-FCT is obtained via a two step form of the Taylor-Galerkin scheme of Donea (1984), which has been used for the computation of inviscid and viscous flows for the Cartesian (Löhner et al. 1989; Baum et al. 1990) and axisymmetric coordinate systems (Löhner et al. 1989; Loth et al. 1990a, 1990b). The Taylor-Galerkin scheme is used to increase the order of the approximation of the time derivative and produce a second order scheme. The spatial discretization is implemented with the usual Galerkin weighted residual method. The scheme involves two steps (Löhner et al. 1985) which together progress the solution from time t^n to time $t^{n+1} = t^n + \Delta t$. Quantities with integer timestep values (t^n and t^{n+1}) are located at nodes and have piecewise linear shape functions, denoted by N_j for a given node j. At the half timesteps, ($t^{n+1/2}$) quantities are centered at the elemental centers and have piecewise constant shape functions for a given element, e. Solution with the consistent mass matrix is achieved by iterating with the lumped mass matrix (Löhner et al. 1984, 1985). For the explicit two step Taylor-Galerkin scheme, a Courant type stability condition (Löhner et al. 1985) is applied to each element to obtain a local time step, Δt_e; from this a maximum CFL number of 0.25 is used for the global timestep.

To formulate the FCT approach, the low order scheme must be monotonic. This has been achieved inexpensively by adding 'mass-diffusion' to the higher order scheme (Löhner et al. 1987), by subtracting the lumped mass matrix from the consistent mass matrix and multiplying this term by the unknowns. The low order solution and the high order solution can then be combined to yield monotonic conditions for the conserved quantities near discontinuities and a second order solution in the rest of the domain, through the FEM-FCT formulation. The six steps of FEM-FCT are defined as (Löhner et al. 1987):

1. Compute the low order element contribution (LEC) from the low order, monotonic scheme.
2. Compute the high order element contribution (HEC) from the high order scheme.
3. Define the anti-diffusive element contribution (AEC), where AEC = HEC - LE.
4. Compute the updated low order solution: U_l^{n+1}.
5. Limit the AEC such that U^{n+1} found in step 6 below is free of extrema not present in U^n or U_l^{n+1}: $AEC^c = C_{el} \cdot AEC$, where $0 \leq C_{el} \leq 1$
6. Apply this limited AEC^c: or $U^{n+1} = U^n + AEC^c$

Crucial to this procedure is the limiting method used to calculate C_{el} in step 5. To maintain strict conservation, this limiting is carried out on the four unknowns ($\rho, \rho u, \rho v$, and ρe) at the elemental level (Löhner et al. 1984). Zalesak (1979) showed that the original limiting method of Boris and Book (1976) needs to be modified for multi-dimensional flow problems. For a system of PDE's such as that in (1), it is typical for one global C_{el} to be chosen in some manner from the individual C_{el}'s of the four unknown fluxes. Unfortunately, no limiter presents itself which is optimum for all flow problems (Löhner et al. 1987). The following is a list of the global limiters investigated in the present study:

1. The global limiter is chosen as the minimum of the limiters from the four unknown fluxes ($\rho, \rho u, \rho v, \rho e$).
2. There is no global limiter; each of the four limiters are kept independent of each other.
3. The global limiter is chosen as the minimum of the limiters for ρu and ρv.
4. Use the average of the four individual limiters for the global limiter.
5. The global limiter is set to the minimum of the limiters for ρ and ρe.

While several approaches to the flux limiting are possible, most previous work with FEM-FCT has included a global limiter on the conservation equations as specified by number 5 above, the minimum of density and energy values (Löhner et al. 1989, 1987; Baum et al. 1990; Loth et al. 1990a, 1990b). However, for the current study it was found that this type of limiter produced non-physical numerical oscillations coming off the upstream surface of the wedge. These oscillations were attributed to a natural local minimum in density and energy which forms on the wedge surface for this low Mach number shock wave. Evidence of this numerical noise was also noted for TVD schemes for similar wedge calculations (Aso et al. 1990). For the above limiters, several boundary conditions at the wedge tip and increased Lapidus diffusion (described below) were employed without success in removing flow oscillations without diffusing the
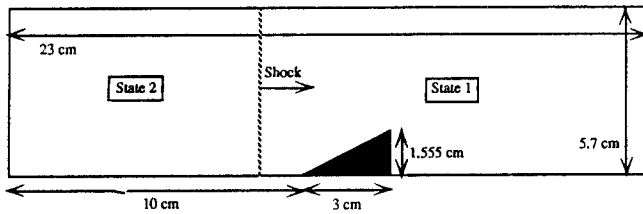
Fig. 1. Numerical domain for the present study

solution, with the exception of employing limiter number 4. It was found that these oscillations could be removed without diffusing the solution significantly by employing a global flux limiter based on the average of the limiters derived by insuring monotonicity of the four unknowns $(\rho, \rho u, \rho v$ and $\rho e)$. Notably, for stronger incident shock speeds, the induced flow behind the shock is supersonic and there is no evidence of these numerical oscillations, presumably since the local minima on the wedge face will no longer exist.

A second type of artificial viscosity was added: Lapidus smoothing (Löhner et al. 1984). The present study employed a Lapidus coefficient of 3 which maintained flux conservation and resulted in shocks and contact discontinuities resolved over typically three and five cells, respectively. A parametric study indicated only a small sensitivity to the value of this coefficient for flowfield features investigated herein.

2.2. Adaptive grid methodology

Adaptive H-refinement was employed to optimize the distribution of grid points by refining areas with high gradients of density or entropy and coarsening areas of low gradients of density and entropy. This allows efficient use of memory and computation time. In general, such refinement may reduce storage and CPU requirements by 10 – 100 times in advection dominated flows as compared to an overall fine grid (Loth et al. 1990a). As in previous studies, a local 'error indicator' was used to determine if a given element needed to be refined, coarsened, of left alone based on the H_2 seminorm.

A separate but similar entropy gradient indicator was used in conjunction with the previously employed density error indicator. This approach differs from many previous computations (Löhner et al. 1987, 1989; Baum et al. 1990; Loth et al. 1990a, 1990b) in that entropy gradients are also considered. This additional flow property was incorporated to enhance the schemes capability to capture slip layers and more importantly, vorticity layers. Results indicated almost a full refinement level increase as compared to density refinement alone for portions of the slip layers and the rolled up vortex region. Such remeshing allows a balanced (and efficient) distribution of truncation errors by controlling the relative size of local computational cells. For the present computation, the following refinement parameters were employed: a minimum size of 0.0028 cm, and a maximum of five levels of refinement, and coefficients of refinement,

deletion, and noise of 0.07, 0.035, 0.035, respectively for both entropy and density.

Boundary conditions consisted of fixed quantities of density, momentum and energy for the inflow conditions; tangental velocity vectors along the wedge surfaces, plane of symmetry, and the upper wall; and free boundary conditions at the top corner and at the outflow boundary. The numerical domain is shown in Fig. 1 to simulate the upper half of the symmetric flowfield of Schardin (1966). All computations were performed on a Cray 2 and required a total of 48 hours of CPU time.

3. Results and discussion

The present computations were completed to simulate the frame by frame shadowgraph measurements of Schardin (1966) at time intervals of 13.6 μs. Frame 2 of Schardin's results is shown in Fig. 2 while Fig. 9 shows the corresponding predicted density contours. The predictions contain 256 contours varying from the minimum of deep blue to the maximum of dark red. The incident shock (marked A in Fig. 9) propagates from left to right, with the reflected wave off the wedge surface propagating as a cylindrical shock (B) centered at the wedge tip. A constant pressure slip layer (C) occurs near the wedge surface, which can also be seen to occur in the experimental results. The triple point is completed by a Mach stem (D) which has begun to diffract around the corner, although the experimental shadowgraph has difficulty picking up the Mach stem. These features are typical of single Mach reflection (Obermeier and Handke 1990) that results from the low shock Mach number and the ramp angle (27.5°). The induced velocity near the wedge tip convects the upstream end of the slip layer further downstream along the wedge surface. The local minimum in the density (which had previously given numerical oscillations) can be seen to occur above the upstream end of the slip layer (C). The numerical mesh contains 39,357 points, including 3 to 4 refinement levels on the slip layer as shown in Fig. 10 (successive levels of refinement are shown as green, yellow, red, white and light blue). This exhibits the advantage of entropy refinement – without the entropy error indicator, the slip layer is refined to typically 3 levels.

Figure 11 represents the flow midway between frames 2 and 3. The incident shock (A) has passed the wedge and the Mach stem (D) has partially diffracted around the corner. The diffraction causes the shock to curve, thus weakening the shock and causing less of an entropy rise as it diffracts, resulting in the formation of an entropy fan (G) starting at the corner and extending downstream to the diffracted part of the Mach stem. A vortex layer is emanating from the corner of the wedge, which has engulfed the vertex of the entropy fan. Velocity vector plots indicate that separation is at the corner, as expected.

Figure 3 shows the experimental results from frame 4 of Schardin, and Fig. 12 examines a close-up of the density contours for that frame. The Mach stem (D) has diffracted around the corner to form a cylindrical shock sending back an expansion fan (E) in the opposite direction, which has
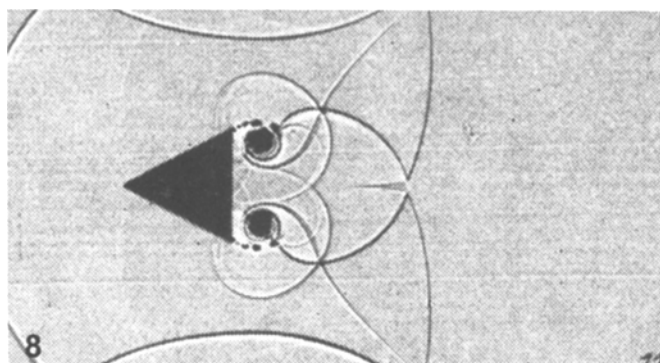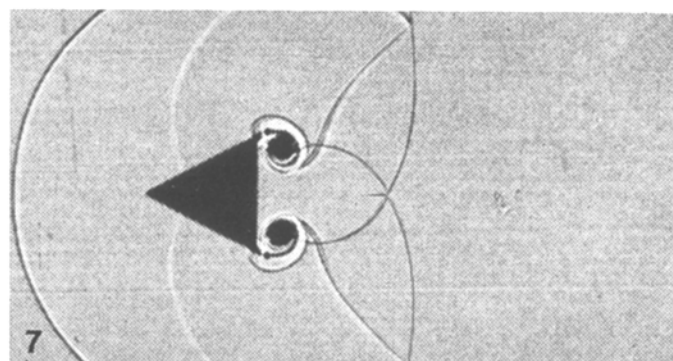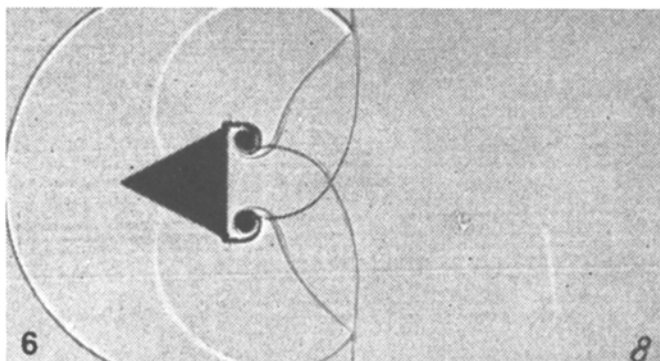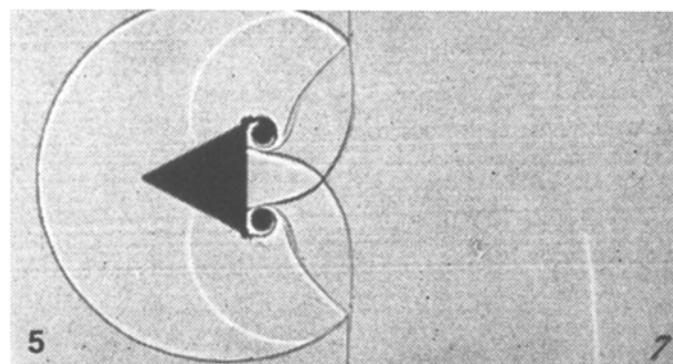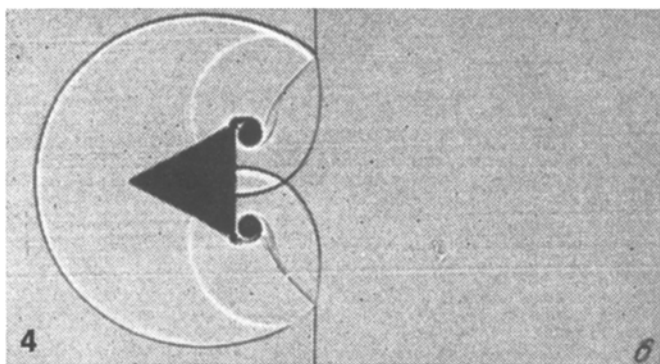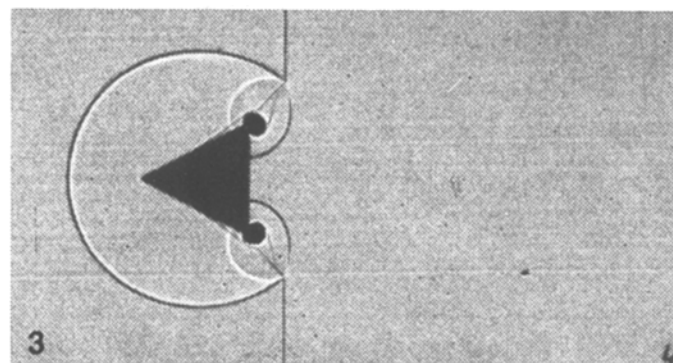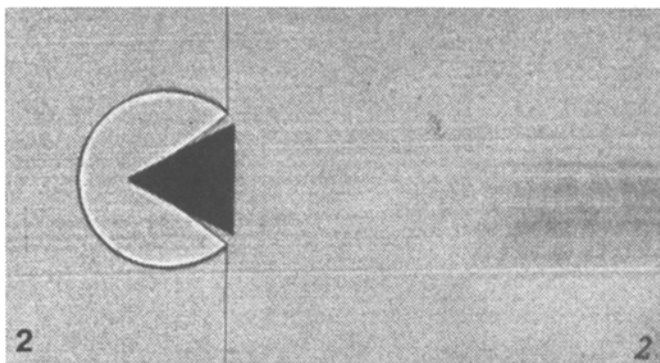
Fig. 2. Frame 2 of Schardin's shadowgraphs

Fig. 3. Frame 4 of Schardin's shadowgraphs

Fig. 4. Frame 6 of Schardin's shadowgraphs

Fig. 5. Frame 7 of Schardin's shadowgraphs

Fig. 6. Frame 8 of Schardin's shadowgraphs

Fig. 7. Frame 9 of Schardin's shadowgraphs

Fig. 8. Frame 11 of Schardin's shadowgraphs

now reached the triple point. The vortex layer has rolled up in a clockwise manner, effectively becoming a single vortex (F), and has begun to deform the slip layer (C). The entropy fan (G) now terminates downstream at the triple point, and its upstream end has curled up with the vortex and is compressed into an entropy layer nearby the vortex. For these frames, the numerical results show excellent agreement with the experimental results due to the enhanced grid adaptation and robust monotonic scheme.

Figures 4 and 13 show Schardin's experimental frame 6 and the corresponding numerical density contours. The experimental results show that the diffracted Mach stems (D) from the upper and lower corners have crossed. The symmetric numerical case represents this crossing as a reflection of the cylindrical shock off the bottom wall (H). The vortex (F) is convecting downward and to the right (downstream). The slip layer (C) continues to deform with the vortex and is nearing the entropy layer (G). The simulation continues to provide excellent agreement with the experimental results.

Figures 5 and 14 show Schardin's experimental frame 7 and the corresponding numerical density contours. One may observe in both figures the upstream movement of the expansion fan (E) which has begun to interact with the initial reflection (B). At this point, the transmitted reflective shock (H) is now just about to interact with the vortex (F), the slip layer (C), and the entropy layer (G). It appears from the predictions that the vortex is already causing some deformation to the reflected shock (H). In principle, the Mach stem diffracting around the corner can be thought of as a localized normal shock diffracting around the corner as was studied by Howard and Mathews (1956) and Merzkirch (1964). However, this analogy breaks down once the slip layer (C) and reflected shock (H) have begun to interact with the vortex flowfield as shown in Fig. 14.

Figure 6 is frame 8 of Schardin's experimental run, while Fig. 15 gives the corresponding predicted density contours for a close-up of the wedge corner. The slip layer (C) has begun to roll up around the vortex and merge with the entropy layer (G). The reflected Mach stem (H) has contacted the vortex (F) and has essentially been split into two shocks. One shock (I) extends from the back face of the wedge to the vortex and the other shock front (H) starts at the vortex and continues downstream. The shock (I) was not picked up by the shadowgraph (as was the case of shock D in frame 1), but later shadowgraphs show its existence. Small timestep video sequencing of the simulation clearly shows the breakup of the reflected shock into I and H; the acceleration I receives owing to the vortex F; as well as the deceleration of H near the vortex as evidenced by its curvature. The shock (I) then passes through the vortex layer and emerges above the layer, and its downstream end diffracts around with the vortex resulting in a weak cylindrical shock at that point. The interaction of the shocks I and H with the vortex layer surrounding F, results in significant increased perturbation and disorganization of the established Kelvin-Helmholtz instabilities. Predicted pressure contours at this point are shown in Fig. 16, which effectively eliminates the slip layers and the entropy layers. The results indicate the robustness of the monotonic scheme in providing sharp discontinuities without oscillations in a complex interaction,

while still maintaining higher order accuracy away from these features.

Figure 7 is the experimental shadowgraph and Fig. 17 is the corresponding density prediction for the ninth frame. By this time, the shock (I) has passed through the vortex layer and emerged above the layer. The end of the shock (I) that projected into the vortex (F) has convected around with the vortex resulting in a cylindrical shock roughly emanating from the vortex center. The reflected Mach stem (H) has apparently formed a triple point at the vortex. Figure 18 shows entropy contours corresponding to frame 9. This figure gives a clear picture of the vortex and its effects on the entropy and slip layers. The slip layer (C) has begun to roll up around the vortex and merge with the entropy layer (G). In addition, the vortex layer instabilities are evident in both the experiment and predictions, and exhibit roughly the same wavelength.

Frame 11 of Schardin's experiment is shown in Fig. 8, with corresponding predictions of density contours in Fig. 19. This initial reflected shock (B) has reflected again off the top wall and is now propagating downward. The diffracted Mach stem (D) has formed a triple point with the reflected Mach stem (H), while above the incident shock has almost been eliminated. By this time, the upstream end of the slip layer (C) has become completely engulfed by the vortex (F), where it follows closely with the entropy layer (G). The Kelvin-Helmholtz instability can be seen in the vortex layer of both experiments and predictions (although, this is more easily observed in predicted vorticity contour plots, Sivier 1991). Mach number predictions indicate supersonic flow (up to Mach 1.2) above the vortex layer terminating at the reflected shock H, as well as in the upper third of the vortex. The shock (I) continues to expand, although the upper portion has lost much of its strength as it expanded upstream. Figure 20 shows the mesh refinement levels for the numerical flow for frame 11 (the mesh at this point contains 143,261 nodes). The primary shocks generally still refine fully to five levels, while the slip layer has lost some refinement at the downstream end as it has weakened.

The above figures have shown that the computational flow features have demonstrated very good agreement with those of the experiment. The numerical results also allow non-intrusive inspection of several highly resolved features which are not accessible or difficult to see in the experimental flow field, such as the origin of the shock (I) and the formation of the entropy fan(G). In addition, quantitative comparison of the numerical results with the experimental results given by Schardin (1966) was also completed. Figure 21 gives a schematic of the flow measurements that were made of both the experimental and numerical result. The quantitative features include:

x – distance from back of wedge to the primary shock (A)

a – horizontal distance from the nose of the wedge to the reflected shock (B)

r – vertical distance from the midline of the wedge to the highest point of the reflected shock (B)
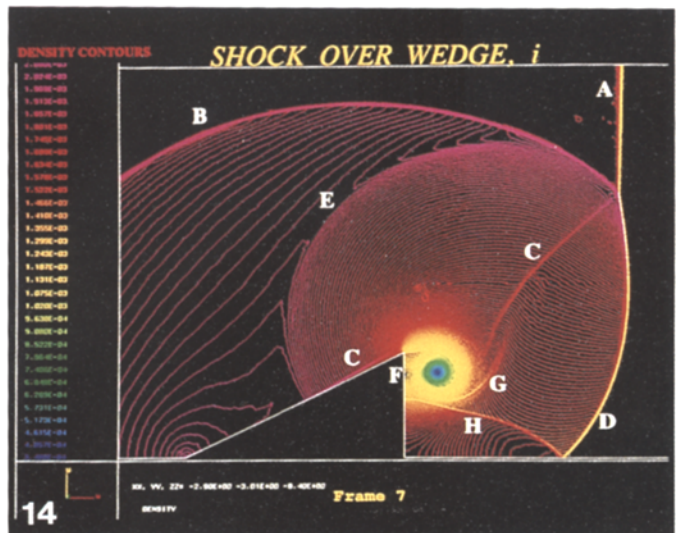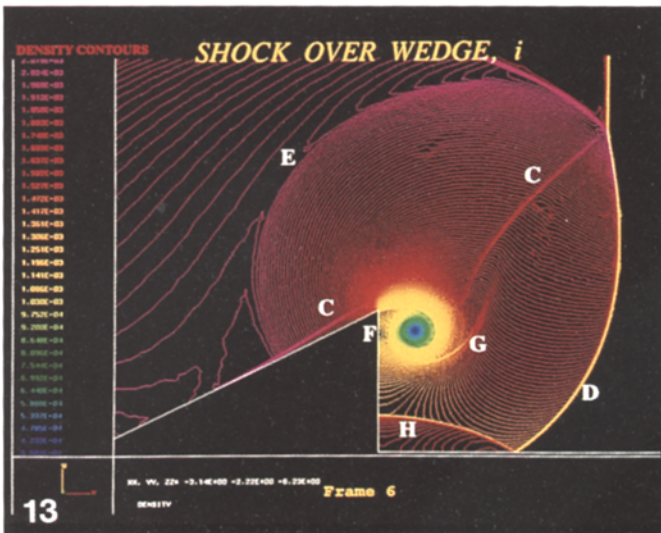
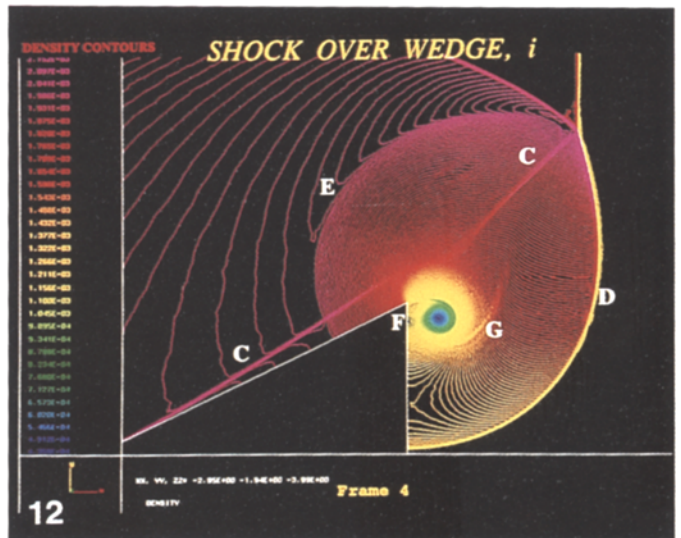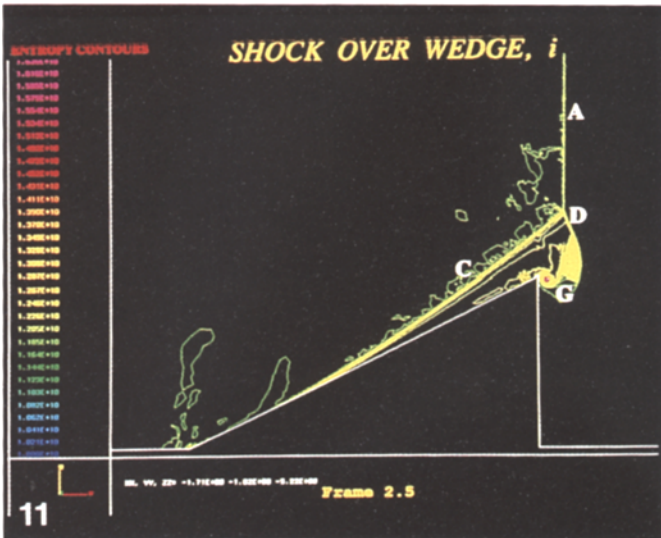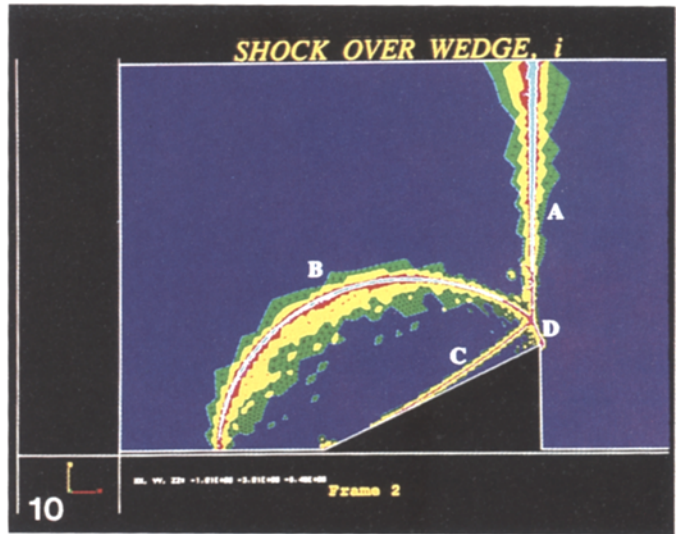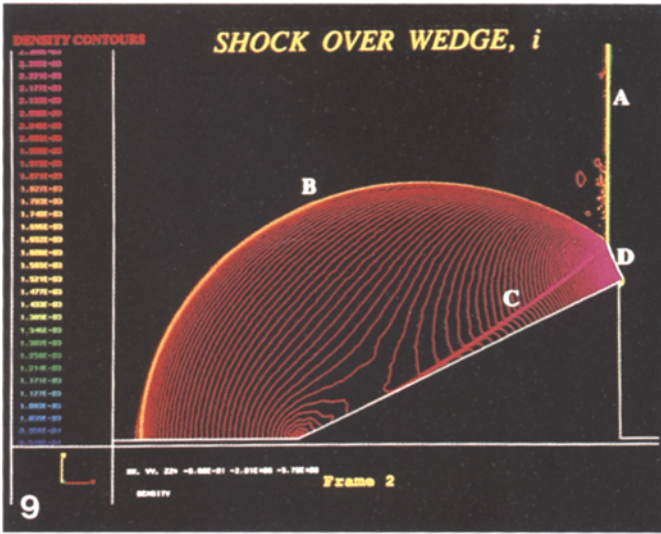b – distance from back of wedge to the triple point formed

Fig. 9. Density contours corresponding to frame 2
Fig. 10. Mesh levels of refinement corresponding to frame 2
Fig. 11. Entropy contours corresponding to frame 2.5
Fig. 12. Close-up of density contours corresponding to frame 4
Fig. 13. Density contours corresponding to frame 6
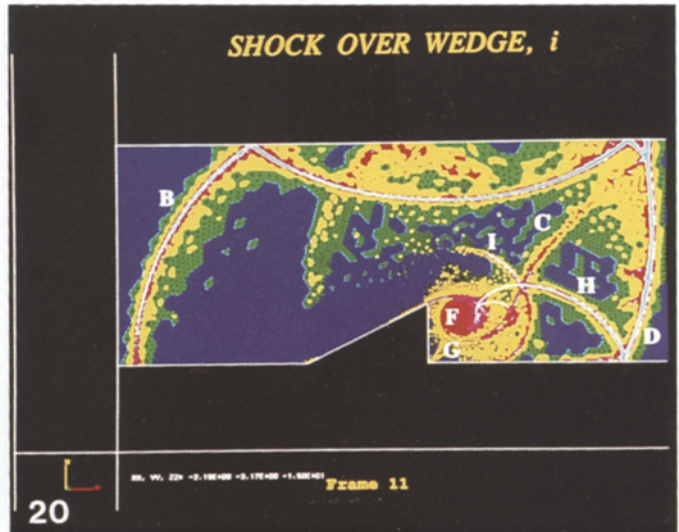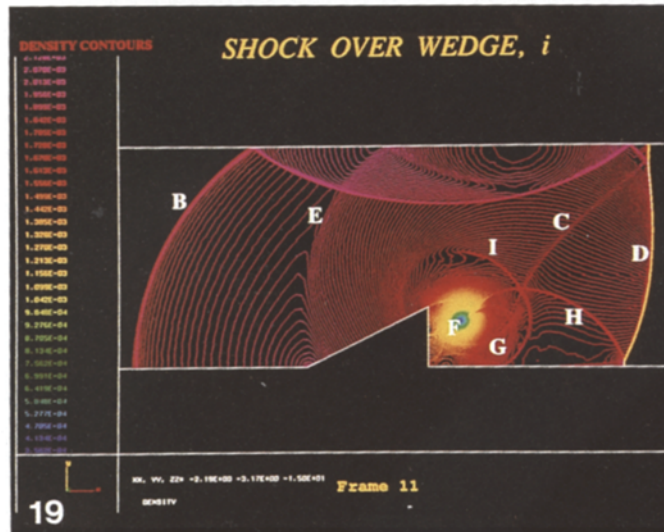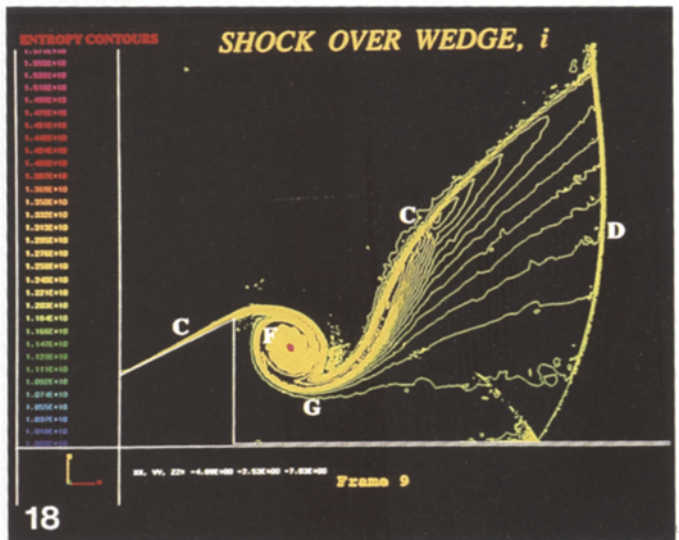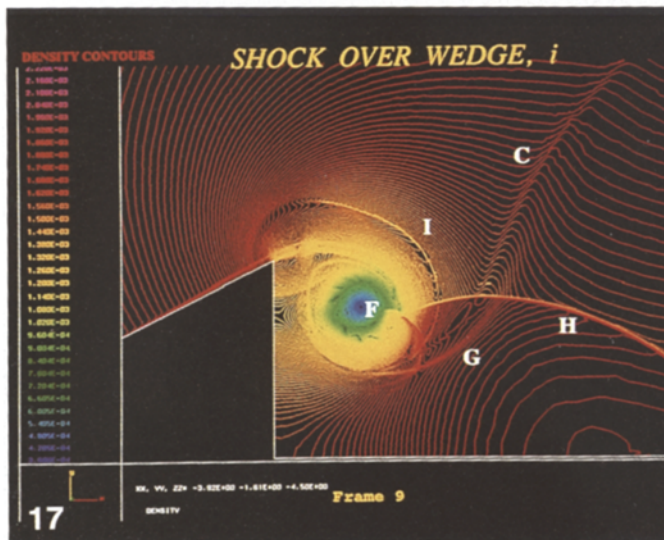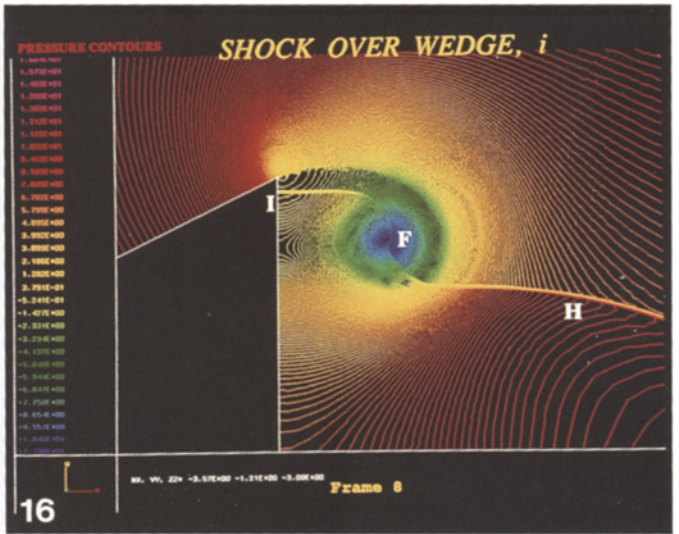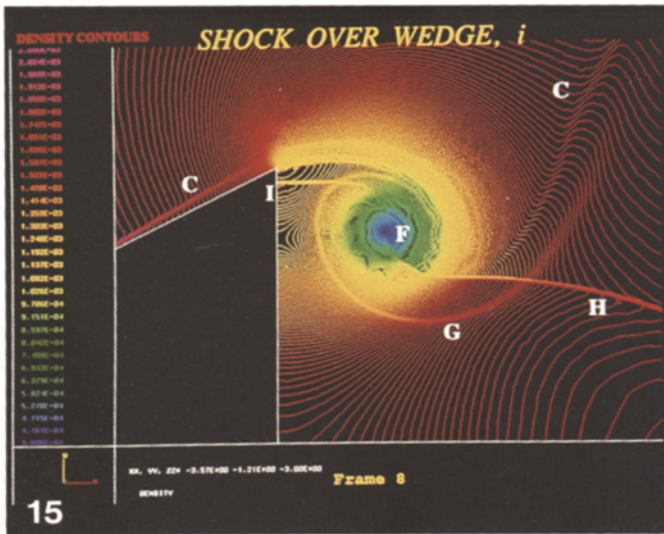Fig. 14. Density contours corresponding to frame 7

Fig. 15. Density contours corresponding to frame 8

Fig. 16. Pressure contours corresponding to frame 8

Fig. 17. Density contours corresponding to frame 9

Fig. 18. Entropy contours corresponding to frame 9

Fig. 19. Density contours corresponding to frame 11

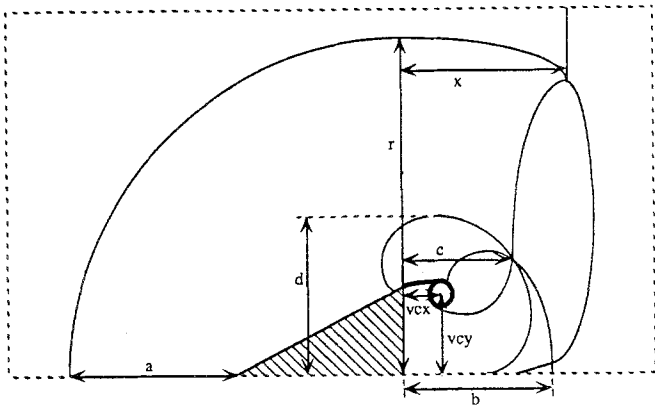Fig. 20. Mesh levels of refinement corresponding to frame 11

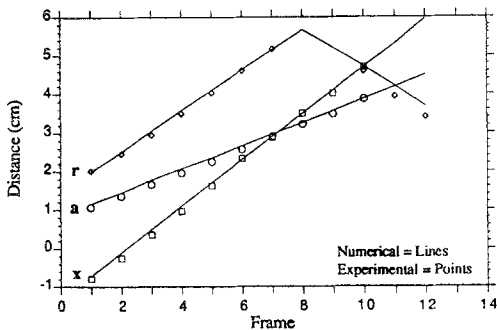Fig. 21. Schematic showing flow measurements

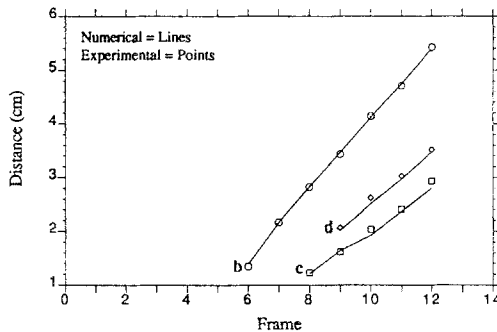Fig. 22. Numerical versus experimental - primary shocks

Fig. 23. Numerical versus experimental - secondary structures

at the intersection of the diffracted Mach stem (D) and its reflected shock (H)

c – distance from the back of the wedge to the intersection of the diffracted Mach stem's reflected shock (H) and the slip layer (C)

d – distance from the midline of the wedge to the highest point of the shock (I)

vcx – distance from the back of the wedge to the geometric center of the vortex (F)

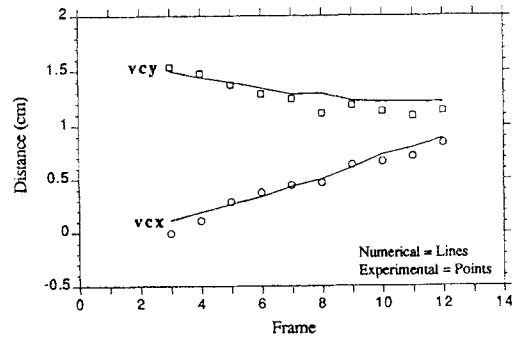vcy – distance from the midline of the wedge to the geometric center of the vortex (F)

Fig. 24. Numerical versus experimental - vortex measurements

Figure 22 shows a comparison of the primary shock locations (measurements r, a and x above). The graph in Fig. 23 compares the positions of the secondary structures (measurements b, c and d above). The numerical results compared extremely well with the experimental results, although the measurement r shows some discrepancy after the reflected shock (B) reflected off the upper wall. This is likely due to a slight inaccuracy in the upper wall position (which had to be estimated).

Figure 24 compares experimental and numerical positions of the vortex (given by measurements vcx and vcy) as it is convected downstream. The comparison, while not as favorable as for the primary shocks and secondary structures, is, never-the-less, still quite good. The rough appearance of the results can be partially explained by the difficulty in locating the center of the vortex (this is made clear by the perturbations of the experimental data). However, the numerical data is fairly linear, the only exception being from frame 7 to frame 9 for vcy. This is precisely the point at which the reflected part of the Mach stem (H) impacts the vortex (F), thereby causing the vortex to temporarily stop its downward motion. By frame 9 this shock has passed the vortex allowing it to renew its downward trend, although at a slower rate. Despite the presence of significant entropy variations noted in the flowfield, the vortex growth is found to be approximately conical in nature as suggested by the theory of Howard and Mathews (1956) until the shock interaction occurs at frame 7.

Other flowfield interrogations include pressure traces along the wedge surface which showed clearly the pressure spikes and decreases of the previously discussed compressible flow features (Sivier 1991). One may assert that if the position and speed of the shocks and vortices are correctly predicted over the wedge surfaces, then the resulting surface pressures should be reasonably modeled.

To test grid dependence, a computation was made with roughly half the number of points, by increasing the allowed minimum element size to keep the number of points below 85,000. Figures 25 and 26 show a comparison of the shock positions and vortex positions for the high and low resolution computations. Both give remarkably similar results. Therefore, the present implementation of the FEM-FCT method and grid adaptation indicates that reasonable grid independence has been achieved for the present computations.
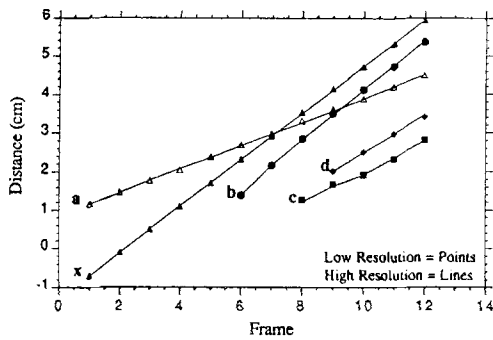
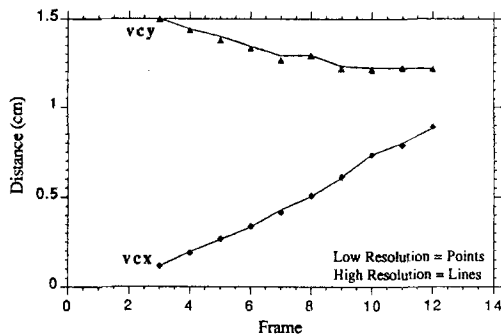Fig. 25. Comparison of mesh resolution - shock position

Fig. 26. Comparison of mesh resolution - vortex position

4. Conclusions

From the above results, it has been shown that the FEM-FCT algorithm provides excellent predictions of a shock wave impinging on a ramp and diffracting past a rearward facing step, both in terms of compressible wave characteristics and sharp corner vorticity generation. The global limiter, based on the average of the limiters of the four unknowns, was shown to be capable of capturing shocks without generating numerical oscillations, including areas where the flow naturally generated local minima. The adaptive grid generation scheme employed density and entropy gradients in order to ensure proper refinement for both weak and strong structures.

The flow was shown to generate a single Mach reflection with a corresponding triple point as the incident shock moved up the ramp. As the shock passed the wedge corner, the Mach stem diffracted, an expansion fan was sent back upstream, and a slip layer formed at the corner, which convected downstream, underwent Kelvin-Helmholtz instabilities and proceeded to curl up to form a vortex. In addition, an entropy fan was formed by the weakening of the Mach stem as it diffracted. As this stem continued down to the midline of the wedge, it reflected back up to interact with the vortex, causing the expulsion of a small cylindrical shock that convected away from the vortex in all directions. Very good agreement was found between the numerical and experimental results in terms of the above

flow features, as well as the shock and vortex trajectories, indicating a reasonable representation of the separated gas dynamics and resulting surface pressures. Thus, the present methodology has provided a high resolution description of the fluid physics associated with shock diffraction, sharp corner vortex production and transport, and shock vortex interaction. Future work will include direct Navier-Stokes simulations to determine the significance of boundary layer effects in this flowfield.

References

Aso S, Hayashi M, Takano M (1990) Numerical simulations of unsteady shock reflection processes by a ramp. In: The proceedings of the Symposium of Mechanics for Space Flight 1989, Tokyo, The Institute of Space and Astronautical Science, March 3-14

Baum JD, Loth E, Löhner R (1990) Numerical simulation of shock interaction with complex geometry canisters. In: Kim Y (ed) Current Topics in Shock Waves, American Institute of Physics, pp 909-914

Ben-Dor G, Glass II (1980) Domains and boundaries of non-stationary oblique shock wave reflexions, II Monatomic gas. J Fluid Mech 96:735-756

Boris JP, Book DL (1976) Flux-corrected transport, III Minimal-error FCT algorithms. J Comp Phys 20:397-431

Donea J (1984) A Taylor-Galerkin method for convective transport problems. Int J Num Methods Eng 20:101-119

Glass II, Kaca J, Zhang DL, Glaz HM, Bell JB, Trangenstein JA, Collins JP (1990) Diffraction of planar shocks over half-diamond and semi-circular cylinders: an experimental and numerical comparison. In: Kim Y (ed) Current Topics in shock Waves, American Institute of Physics pp 246-251

Glaz HM, Colella P, Glass II, Deschambault RL (1985) A numerical and experimental study of pseudo-stationary oblique shock wave reflections in air and argon. Proc R Soc Lond A 398:117-140

Heilig W, Reichenbach H (1983) About the trend of pressure in shock reflection processes. In: Archer RD, Milton BE (eds) Proc of the 14th Int Symp Shock Waves and Shock Tubes pp 151-158

Howard L, Mathews D (1956) On the vortices produced in shock diffraction. J Appl Phys 27:223-231

Löhner R, Morgan K, Zienkiewicz OC (1984) The solution of non-linear hyperbolic equation systems by the finite element method. Int J Num Meth Fluids 4:1043-1063

Löhner R, Morgan K, Zienkiewicz OC (1985) An adaptive finite element procedure for high speed flows. Comp Meth Appl Mech eng 51:441-465

Löhner R, Morgan K, Peraire J, Vahdati M (1987) Finite element flux corrected transport (FEM-FCT) for the Euler and Navier-Stokes equations. Int J Num Meth Fluids 7:1093-1109

Löhner R, Baum JD, Loth E, Ramamurti R (1989) A finite element solver for axisymmetric compressible flows. AIAA-89-1794, 20th Fluid Dynam Plasma Dynam Lasers Conf, Buffalo NY, June 12-14

Loth E, Baum JD, Löhner R (1990a) Formation of shocks within axisymmetric flows. AIAA-90-1655 21st Fluid Dynam Plasma Dynam Lasers Conf Seattle WA, June 15-18

Loth E, Kailasanath K, Löhner R (1990b) Supersonic flow over an axisymmetric backward facing step. AIAA-90-1580 22nd Fluid Dynam Plasma Dynam Lasers Conf Seattle WA June 15-18

Mandella M, Moon YJ, Bershader D (1985) Quantitative study of shock-generated compressible vortex flows. In: Bershader D, Hanson R (eds) Proc 15th Int Symp Shock Waves and Shock Tubes pp 471-477

Meadows KR, Kumar A, Hussaini MY (1991) Computational study on the interaction between a vortex and a shock wave. AIAA J 29:174-179

Merzkirch W (1964) Theoretische und Experimentelle Untersuchungen an einer instationaren Wirbelstromung. Zeit Flugwissen 12:395-401

Obermeier F, Handke E (1990) Unsteady Mach reflection of weak shock waves. In: Kim Y (ed) Current Topics in Shock Waves, American Institute of Physics pp 84-95

Schardin H (1957) High frequency cinematography in the shock tube. J Photo Sci 5:19-26

Schardin H (1966) Stossrohre [Shock Tubes]. Oertel H (ed) Springer Verlag NY pp 716-720

Sivier SA (1991) Vorticity produced by shock wave diffraction. Masters Thesis, Uni Ill at Urbana-Champaign

Zalesak ST (1979) Fully multidimensional flux-corrected transport algorithms for fluids. J Comp Phys 31:335-362